Journal of
Composites Science

MDPI

Article

Design, Manufacturing, and Analysis of a Carbon Fiber Reinforced Polymer Crash Box

Mehmet Engul [1,2,*], Serdar Demir [2,3] and Nuri Ersoy [2]

[1] Department of Mechanical Engineering, Virginia Tech, Blacksburg, VA 24061, USA
[2] Department of Mechanical Engineering, Boğaziçi University, Istanbul 34342, Turkey
[3] Department of Mechanical Engineering, Yildiz Technical University, Istanbul 34220, Turkey
* Correspondence: mehmetce@vt.edu

Abstract

This paper presents a novel carbon fiber reinforced polymer (CFRP) crash box design, incorporating numerical analysis and manufacturing aspects. Within the design and analysis phases, a novel numerical methodology is employed to mitigate computational costs in estimating specific energy absorption (SEA). The proposed approach involves a reduction in ply interfaces and modification of pertinent material properties to optimize energy dissipation, achieving more than 50% reduction in simulation time. This methodology is applied to the design of a composite crash box made of unidirectional (UD) carbon/epoxy prepregs, resulting in a new geometry: sun-like shape featuring four sinusoidal arms connected to a central circular core. Subsequent manufacturing and testing reveal a SEA value of 79.46 J/g for designed geometry, surpassing metallic counterparts by a factor of 3 to 4. Furthermore, this study conducts a comparative analysis of energy absorption performance between unidirectional and woven fabric prepregs for the same geometry. Utilizing carbon/epoxy woven fabric (WF) prepregs further enhances the SEA to 89.26 J/g. Finally, the application of edge tapering to the crash box structure is shown to eliminate initial peak loads, thereby preventing excessive deceleration.

Keywords: polymer composites; specific energy absorption; finite element model; crash box

1. Introduction

Crash boxes are the structural components placed at the front crash zones of vehicles. During a crush event, they are expected to collapse and absorb as much crash energy as possible so that the damage of the main frame is minimized. These structures should also be light in weight. Metallic structures which are still widely used as crash boxes have a specific energy absorption (SEA) between 15 and 30 J/g [1,2]. The amount of energy absorbed by the unit mass can be increased significantly by applying lightweight alternatives such as carbon fiber reinforced plastic (CFRP) composites. CFRP structures are known to display better energy absorbing capabilities compared to metallic ones. Moreover, they can offer numerous benefits including strength, weight reduction, and design flexibility.

Among numerous factors, geometry significantly impacts the energy absorption capacity of composite crash boxes. Over the years, extensive research has focused on examining the energy absorption performance of various composite geometries. Both experimental and numerical investigations in this field highlight composite tubes as the most thoroughly explored geometries for crashworthy components [3–10]. In separate investigations, Kindervater [6] and Mamalis et al. [7] independently demonstrated the superior energy

Check for updates

Academic Editor: Haifeng Zhao

Received: 15 December 2025
Revised: 18 January 2026
Accepted: 31 January 2026
Published: 6 February 2026

Copyright: © 2026 by the authors. Licensee MDPI, Basel, Switzerland. This article is an open access article distributed under the terms and conditions of the Creative Commons Attribution (CC BY) license.

absorption capabilities of circular composite tubes compared to square tubes of equivalent cross-sectional area. Farley et al. [8] noted an inverse correlation between the diameter-to-thickness ratio and the specific energy absorption (SEA) of circular tubes. As tubes transition towards more elliptical shapes, their SEA performance tends to improve [9]. Hussain et al. [10] examined the crashworthiness of GFRP decagonal structures, revealing higher SEA values compared to circular and elliptical crash boxes. Corrugated designs such as sinusoidal geometries are known to improve energy absorption capability to a considerable extent. Among the few studies investigating the crushing behavior of sinusoidal specimens, Hanagud et al. [11] and Wiggenraad et al. [12] were the pioneers in conducting comprehensive experimental tests on sinusoidal beams, demonstrating their significant potential for energy absorption. Sokolinsky et al. [13] validated the numerical analysis of the crushing response of carbon/epoxy corrugated sinusoidal plates with the experimental data. Engül et al. [14,15] conducted a holistic study investigating the influence of geometry on the SEA of composite structures made of carbon fiber/epoxy unidirectional (UD) and woven fabric (WF) prepregs through different geometries. In these studies, various sinusoidal structures with different amplitudes and number of repeating semi-circle segments were analyzed numerically and experimentally. As depicted in Figure 1, a sinusoidal structure having five semi-circle segments (each of them has 9 mm radius) gives the highest SEA outcome among other geometries which can be considered as part of a complex crash box design.

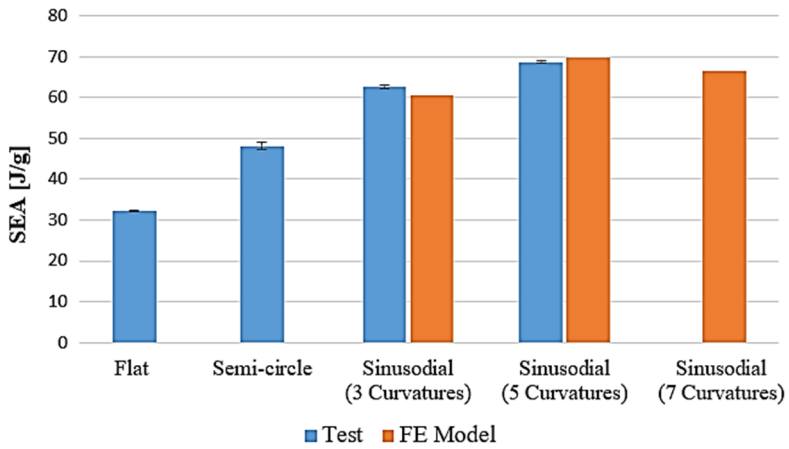

Figure 1. The comparison of SEA performances of several CFRP geometries [14].

Shifting focus from sinusoidal plates, researchers have explored the design of more complex crash boxes to enhance energy absorption capabilities, including I- and H-sectioned beams [16,17] and multi-cell structures [18,19]. The incorporation of T-joints in these structures mitigates delamination, resulting in increased fiber fracture and consequently higher energy absorption. However, due to the predominance of flat walls in their main bodies, the overall specific energy absorption (SEA) of these structures remains inferior to that of sinusoidal structures. The studies conducted thus far indicate that superior SEA performance can be achieved through the design and implementation of more intricate crash box geometries.

This study aims to introduce a novel design that integrates multiple sinusoidal plates forming T-joints between adjacent components. Given that the design process based on trial and error through manufacturing and testing is both time-consuming and costly, the finite element (FE) model predictions play a significant role. However, FE model estimations require high computational time due to the complexity of the failure mechanisms occurring during the crushing process of composite structures. Authors [20] previously proposed a novel numerical approach for flat plates subjected to axial crushing where the

computational cost is decreased by more than 50% by reducing the number of cohesive interfaces between plies and modifying the relevant properties according to a procedure. In this study, this novel modeling approach is applied and validated for the sinusoidal plates. This validation ensures its suitability for the modeling and design of more complex composite structures while enabling significantly reduced computational time. For the design process, three different geometries are proposed in which multiple sinusoidal structures are combined in different configurations. To understand the influence of material type on energy absorption capability, the geometry designed to exhibit the highest specific energy absorption (SEA) is manufactured and tested using both carbon/epoxy woven fabric (WF) prepregs and unidirectional (UD) fibers. As a final design refinement, edge tapering is introduced to the designed crash box structure to effectively reduce the initial peak load and prevent excessive deceleration.

2. Validation of the Numerical Approach

2.1. Numerical Analysis

The novel modeling approach developed for $[0/90]_{2s}$ flat plates involves extruding four [0/90] sub-laminates with one element through the thickness, instead of modeling eight individual plies, thereby reducing the number of interfaces from seven to three [20]. To balance energy dissipation, this method requires a preliminary modeling procedure that includes the application of three-point bending models first to 0 and 90-degree individual plies, then to the [0/90] sub-laminate. The difference between the sum of the total absorbed energy value obtained from two single models and the value obtained from a single sub-laminate indicates the extent of the decrease in intralaminar properties. It is observed that the total energy dissipation of the individual plies is higher than that absorbed by bending a sub-laminate. For the cross-ply plates, consistent results from this novel approach were obtained by halving the in-plane parameters. Additionally, the reduction in the number of interfaces necessitated doubling the fracture toughness values to balance energy dissipation via delamination. Meanwhile, the interfacial strength values increased by 41% to keep the cohesive zone length constant. The proposed approach enables the prediction of SEA and load–displacement responses without sacrificing the identification of the dominant damage mechanisms. In fact, the combined modification of plies and intralaminar properties allows the underlying damage mechanisms to remain reasonably consistent with the physical behavior observed in experiments. Thus, the modeling strategy allows not only the SEA results but also the reproduction of load–displacement curves that show good agreement with experimental results. A detailed description and validation of the numerical method, applied to flat plate structures, can be found in the authors' previous study [20].

This paper uses the same numerical model for simulating the sinusoidal structures to demonstrate its applicability to complex geometries. An FE model in Abaqus/Explicit is applied for AS4/8552carbon/epoxysinusoidal structures with 3 and 5 curvatures by modelling half of the geometry. Figures 2 and 3 show the developed ABAQUS/CAE models. An artificial plug-initiator is utilized in FE models to initiate delamination properly and create a V-shape area to simulate the debris wedge formation during testing. The numerical results of the novel method are compared in the results section with experimental data previously obtained by the authors [14].

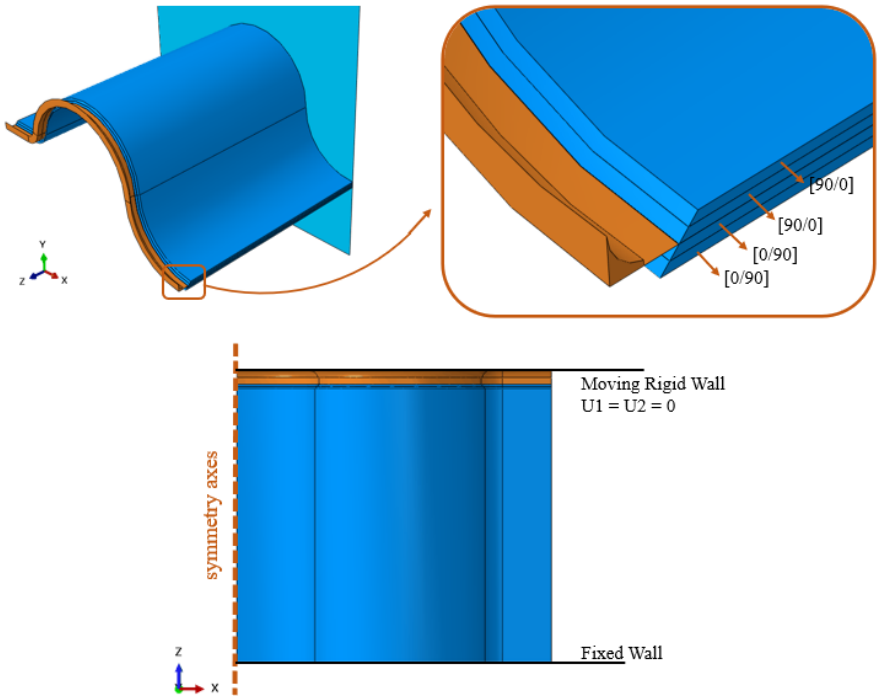

Figure 2. Novel FE model of $[0/90]_{2s}$ sinusoidal structures with 3 curvatures.

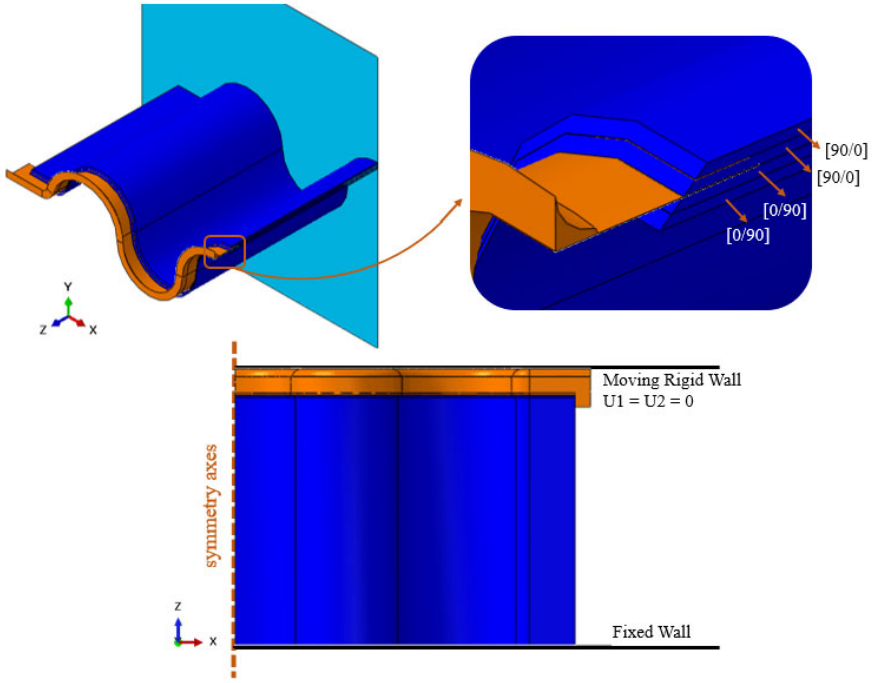

Figure 3. Novel FE model of $[0/90]_{2s}$ sinusoidal structures with 5 curvatures.

For the simulation of the crushing process of composite sinusoidal structures, a progressive failure model is developed by using ABAQUS/Explicit software (Version 6.). Each [0/90] sub-laminate is individually meshed with continuum shell elements (SC8R). Figures 2 and 3 demonstrate the boundary conditions applied in the FE model to be coherent with experimental data. The intralaminar damage initiation due to both fiber and matrix cracking is modeled using the Hashin criteria [21]:

$$\text{Tensile fiber failure for } \sigma_{11} \geq 0 \quad \left(\frac{\sigma_{11}}{X_T}\right)^2 + \alpha\left(\frac{\sigma_{12}}{S}\right)^2 \geq 1 \tag{1}$$

$$\text{Compressive fiber failure for } \sigma_{11} < 0 \quad \left(\frac{\sigma_{11}}{X_C}\right)^2 \geq 1 \tag{2}$$

$$\text{Tensile matrix failure for } \sigma_{22} > 0 \quad \left(\frac{\sigma_{22}}{Y_T}\right)^2 + \alpha\left(\frac{\sigma_{12}}{S}\right)^2 \geq 1 \tag{3}$$

$$\text{Compressive matrix failure for } \sigma_{22} < 0 \quad \left(\frac{\sigma_{22}}{2S}\right)^2 + \left[\left(\frac{Y_C}{2S}\right)^2 - 1\right]\frac{\sigma_{22}}{Y_C} + \left(\frac{\sigma_{12}}{S}\right)^2 \geq 1 \tag{4}$$

where σ_{11}, σ_{22}, and σ_{12} symbolize normal stresses in fiber and transverse directions and shear stress. $\boldsymbol{X_T}$ and $\boldsymbol{X_C}$ symbolize tensile and compressive strength in the fiber direction, while $\boldsymbol{Y_T}$ and $\boldsymbol{Y_C}$ are tensile and compressive strength in the transverse direction. **S** is the shear strength value. Degradation of material stiffness characterizes the damage evolution behavior, which is computed from:

$$C_d = \frac{1}{D}\begin{bmatrix} (1-d_1)E_{11} & (1-d_1)(1-d_2)v_{21}E_{11} & 0 \\ (1-d_1)(1-d_2)v_{12}E_{22} & (1-d_2)E_{22} & 0 \\ 0 & 0 & (1-d_{12})G_{12}D \end{bmatrix} \tag{5}$$

where $D = 1-(1-d_1)(1-d_2)v_{12}v_{21}$. E_{11} and E_{22} denotes Young's modulus in fiber and transverse directions. G_{12} is the shear modulus, and v_{12}, v_{21} represent Poisson's ratios. d_1, d_2, and d_{12} symbolize the current state of fiber, matrix, and shear damages ranging from 0 to 1. In Abaqus/Explicit, an element is not deleted until all three damage parameters reach 1 at the same time. An undeleted element that has already undergone one type of damage can still carry some load, which may have a negative influence on the crushing morphology observed during the process. On the other hand, aside from introducing an additional fluctuation in the load–displacement curve, it is seen in this study that undeleted elements have no significant effect on energy absorption performance.

Interlaminar failure is applied by using the Cohesive Zone Model (CZM) in which mixed-mode delamination (both opening and shearing modes) onset and propagation is considered [22,23]. By utilizing the relation between the cohesive surface tractions and separations, the delamination initiation is determined by the quadratic formula, as can be found in Equation (6). The cohesive damage softening behavior is modeled with a linear softening law that incorporates mixed-mode fracture energy criteria based on the Power Law (Equation (7)).

$$\left(\frac{\sigma_{\mathrm{I}}}{\tau_{\mathrm{I}}}\right)^2 + \left(\frac{\sigma_{\mathrm{II}}}{\tau_{\mathrm{II}}}\right)^2 + \left(\frac{\sigma_{\mathrm{III}}}{\tau_{\mathrm{III}}}\right)^2 = 1 \tag{6}$$

$$\left(\frac{G_{\mathrm{I}}}{G_{\mathrm{I}}^c}\right)^{\propto} + \left(\frac{G_{\mathrm{II}}}{G_{\mathrm{II}}^c}\right)^{\propto} + \left(\frac{G_{\mathrm{III}}}{G_{\mathrm{III}}^c}\right)^{\propto} = 1 \tag{7}$$

where τ_{I}, τ_{II}, and τ_{III} are interfacial strength values of Mode I, Mode II, and Mode III. G_{I}^c is normal fracture toughness; G_{II}^c and G_{III}^c are shear fracture toughness values for Mode II and Mode III, respectively. G_{I} is the normal strain energy release rate, and G_{II} and G_{III} are shear strain energy release rates for Mode II and Mode III. Table 1 lists the material input properties of AS4/8552 composite required for an accurate intralaminar and interlaminar failure in elements having 1 mm mesh size [14,20]. The friction coefficient between the composite specimen and the rigid wall was set to 0.3, following the recommendations of Sokolinsky et al. [13]. Although the experimental tests were conducted under quasi-static conditions (1 mm/min), the ABAQUS/Explicit simulations employed a velocity of 200 mm/s together with a mass scaling factor [24] of 10^2 in order to reduce computational cost. To ensure that quasi-static conditions were preserved, the simulations were designed such that inertial effects remained negligible, as verified by maintaining a low kinetic-to-internal energy ratio throughout the crushing process. In addition, similar modeling

strategies and detailed sensitivity analyses for the influence of velocity and the mass scaling have been previously applied in the authors' previous studies [10,14,15]. Moreover, Sokolinsky et al. [13] also reported that loading velocities below 500 mm/s and mass scaling factors up to 10^3 can be employed without compromising the mechanical response in progressive crushing simulations. On this basis, the adopted choices are considered appropriate for the present study.

Table 1. The material properties of AS4/8552 composite used in the numerical model [14,20].

Description	Unit	Variable	Value
Density	g/cm^3	P	1.58
Longitudinal Modulus	GPa	E_{11}	141
Transverse Modulus	GPa	$E_{22} = E_{33}$	9.75
Principal Poisson's Ratio	-	v_{12}	0.267
Shear Moduli in 1–2 Plane	GPa	$G_{12} = G_{13}$	5.2
Shear Moduli in 2–3 Plane	GPa	G_{23}	3.19
Longitudinal Tensile Strength	MPa	X_T	1100
Longitudinal Compressive Strength	MPa	X_C	750
Transverse Tensile Strength	MPa	Y_T	40
Transverse Compressive Strength	MPa	Y_C	130
In-plane Shear Strength	MPa	S	40
Interfacial Strength (Mode I)	MPa	τ_I	49.3
Interfacial Strength (Mode II and III)	MPa	$\tau_{II} = \tau_{III}$	98.7
Fracture Toughness (Normal)	[kJ/mm^2]	G_{Ic}	0.56
Fracture Toughness (Shear)	[kJ/mm^2]	$G_{IIc} = G_{IIIc}$	5.08

2.2. Results

The load–displacement and the energy results obtained from the novel FE model applied for the $[0/90]_{2s}$ sinusoidal specimen with 3 and 5 curvatures are compared with the experimental data as can be seen from Figure 4. The experimental results were adopted from the authors' previous study [14], in which three specimens were tested for each configuration and exhibited only limited scatter; in the present work, the experimental curve closest to the average response was selected for comparison. Figure 5 gives the deformed shapes obtained at the end of the simulation.

Table 2 summarizes the SEA results and run time values obtained at the end of the simulations. The results demonstrate that the proposed numerical approach is capable of consistently predicting the SEA of the sinusoidal structure while achieving a substantial reduction in computational time. These findings indicate that the cost-efficient methodology, originally developed and validated for flat plate configurations, can be effectively extended to the design and assessment of more complex geometries.

Table 2. SEA results for sinusoidal geometries and the reduction percentages in run time.

Geometry	SEA [J/g] (Test [14])	SEA [J/g] (Conventional FE [14])	SEA [J/g] (Novel FE)	Run Time [h] (Conventional)	Run Time [h] (Novel)	Reduction in Run Time
3-Curvature	62.64	60.84	61.91	4.02	2.17	46%
5-Curvature	68.73	69.7	69.82	4.52	2.3	49%

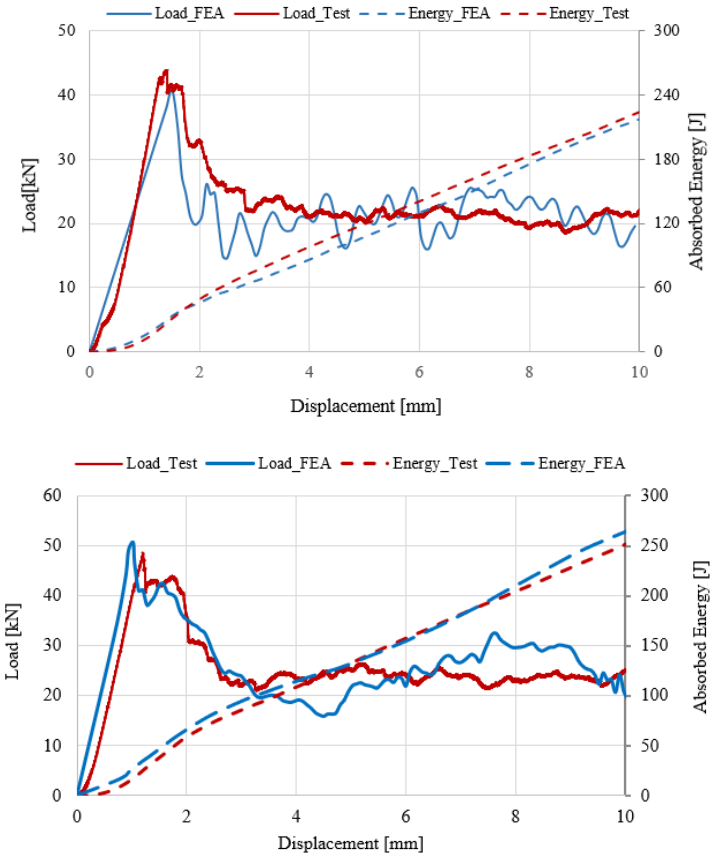

Figure 4. Comparison of the novel FE model of sinusoidal structure having 3 curvatures (**top**) and 5 curvatures (**bottom**) with experimental tests in terms of load–displacement and energy curves.

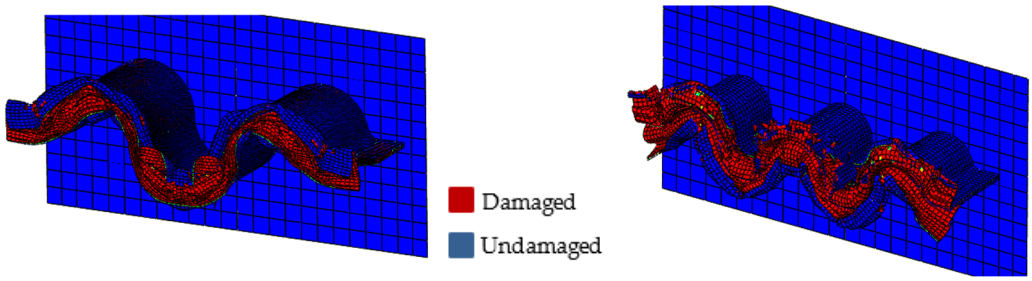

Figure 5. Deformed shapes of sinusoidal specimens with 3 curvatures (**left**) and 5 curvatures (**right**).

3. CFRP Crash Box Design Made of UD Prepregs

3.1. Design and Numerical Analysis

The design concept of the complex crash box structure is based on combining sinusoidal plates (the geometry that exhibited the highest SEA in a previous study [14], each featuring five curvatures with 9 mm radii) by using T-shaped joints. Table 3 presents the cross-sectional views of three alternative designs. Each successive design iteration aims to enhance the specific energy absorption (SEA) characteristics over the previous one. The first geometry, termed "Parallel Sinusoidal Plates (PSP)," combines two sinusoidal structures with two vertical flat components, incorporating four T-joints. Given that curvatures significantly increase energy absorption compared to flat components, the second design features a circular core with four bisected sinusoidal arms connected via T-shaped joints. This design is referred to as the "Sun-like Shape (SL4)." In the final design, the impact of adding more bisected sinusoidal arms to the circular core was assessed, leading to the "Sun-like Shape (SL8)" with eight half-arms.

Table 3. Three crash box designs (all dimensions are given in mm).

Name	Code	Geometry
Parallel Sinusoidal Plates	PSP	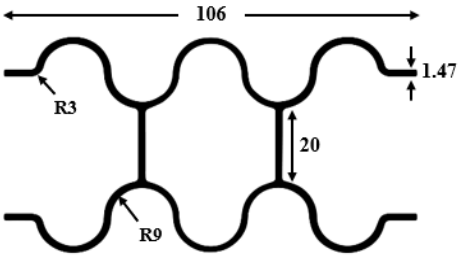
Sun-like Shape With 4 Half Sinusoidal Arms	SL4	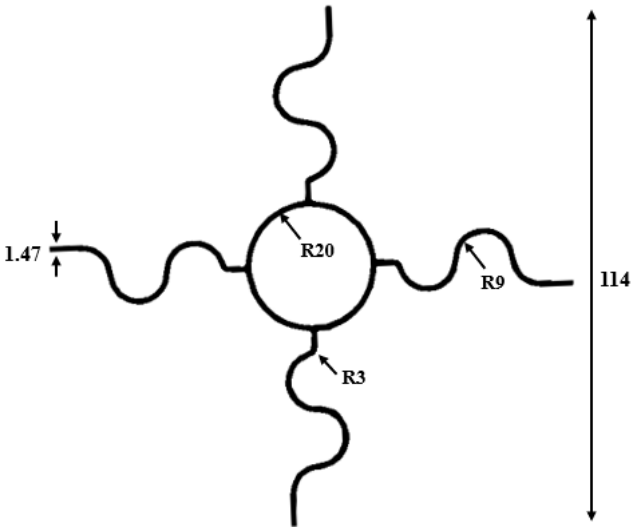
Sun-like Shape With 8 Half Sinusoidal Arms		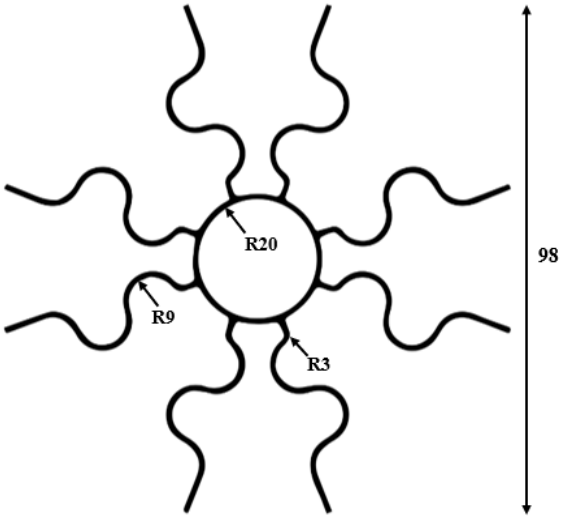

A validated modeling approach is applied to three crash box geometries made of AS4/8552 carbon/epoxy unidirectional (UD) prepregs. In the numerical analysis, the "Parallel Sinusoidal Plates (PSP)" design is first examined by modeling one quarter of the geometry with the plug initiator, as described in the previous section. In this model, each of the four sub-laminates is meshed with continuum shell elements (SC8R) at a 1×1 mm size. The imposed velocity and boundary conditions are consistent with the sinusoidal model presented earlier. Figure 6 illustrates the Abaqus/CAE model, highlighting the trigger mechanism and plug initiator. A V-shaped trigger is incorporated at the edge where the

plug initiator is expected to impact. Figure 7 provides a close-up view of the V-shaped trigger and the lay-up configuration throughout the thickness.

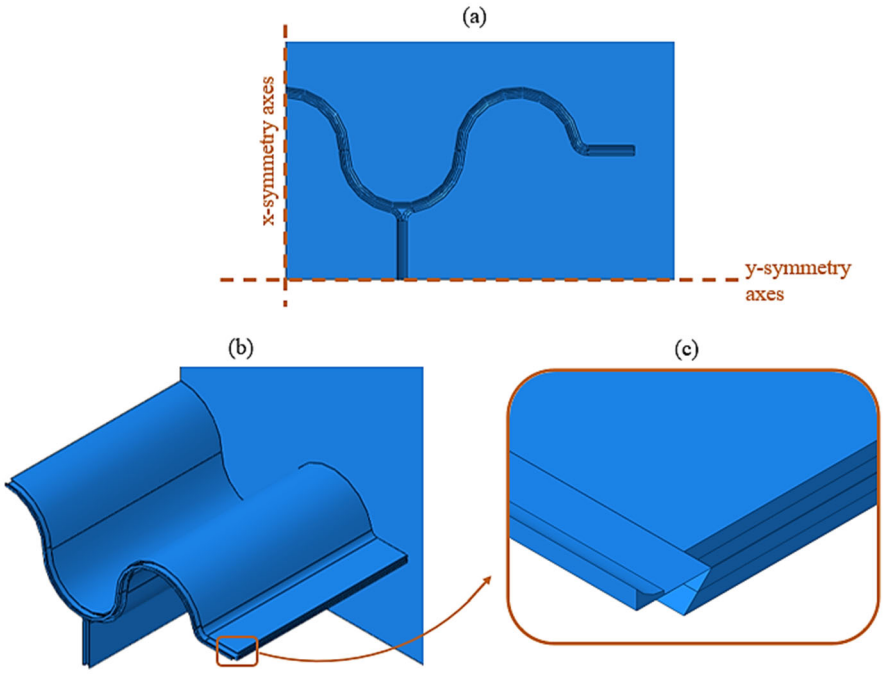

Figure 6. Abaqus/CAE model of PSP geometry: (**a**) front view with symmetry axes, (**b**) isometric view, (**c**) one edge with plug initiator.

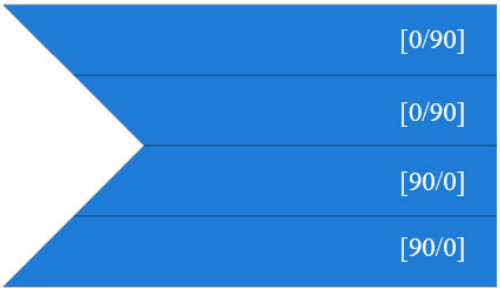

Figure 7. The schematic representing four layers and V-shaped trigger.

Following the numerical analysis of the PSP geometry, FE models for the SL4 and SL8 geometries are also developed using the same approach, trigger mechanism, and conditions (see Figure 8). The numerical analysis of the SL8 geometry is conducted using a quarter model due to its symmetrical properties, whereas the SL4 geometry, lacking any symmetry planes, was analyzed using a full-geometry model.

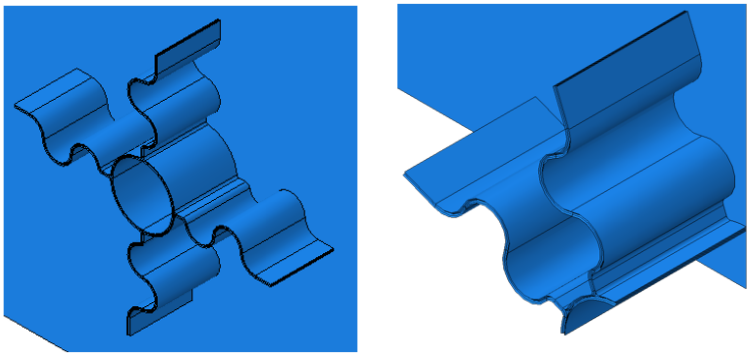

Figure 8. Abaqus/CAE models of SL4 (**left**) and SL8 (**right**) geometries.

3.2. Results of Numerical Analysis

The simulation results with the crushing modes of the PSP geometry are presented in Figure 9, in which fiber, matrix damage, and delamination are demonstrated. As can be seen from the figure, there is intense fiber damage observed in the regions close to the contact zone where delamination has already occurred. The sinusoidal parts at the top and the bottom also exhibit vertical ruptures due to the intense matrix failures. However, there is no matrix damage occurring on the sidewalls of the flat parts positioned at the center, which is estimated to lower the SEA performance. The load–displacement curve obtained at the end of the simulation is presented in Figure 10.

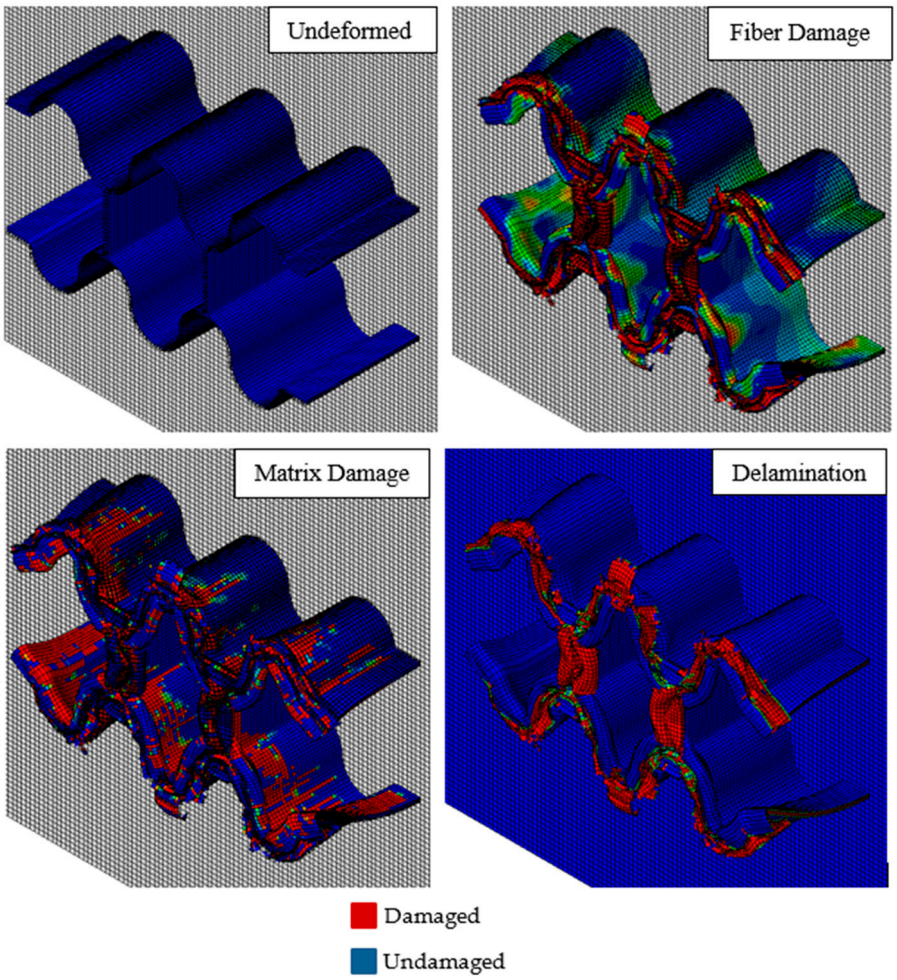

Figure 9. Simulation results of PSP geometry.

The crushing modes derived from the FE model developed for the SL4 geometry are depicted in Figure 11. The load–displacement curve obtained by simulation is illustrated in Figure 12. During the experimental tests, it is not possible to observe, discuss, and distinguish the crush-induced damage mechanisms in detail since they are developing at the same time and in a complex manner. Numerical analyses, at that point, lead to clearer interpretations of the damage mechanisms and their relationship with energy absorption capability. Looking at the simulation results of SL4 geometry with this perspective, in addition to fiber failure and delamination in regions near the contact zone, matrix failure is also evident in the middle plies and sidewalls of the sinusoidal and circular components. As previously discussed, the placement of a circular core at the region's center was anticipated to enhance SEA performance. Simulation results validate this expectation, as evidenced by increased vertical ruptures, micro-buckling, and fiber damage observed in the circular

region. Moreover, tracking the number of damaged elements can also explain why SL4 geometry exhibits more energy absorption than the previous geometry. The number of elements subjected to fiber failure are higher in SL4 geometry than PSP design. Considering that fiber fractures are the most energy absorbing mechanism, this increase in SEA result can be considered relevant.

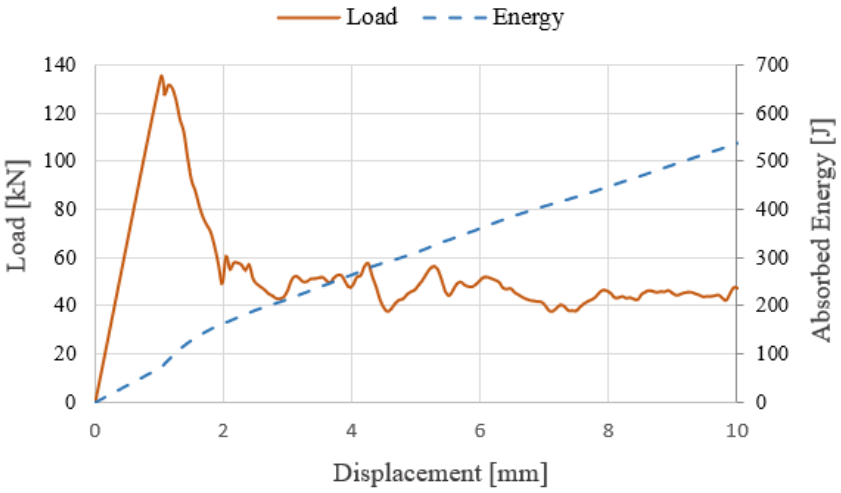

Figure 10. Load–displacement and energy curves of PSP geometry.

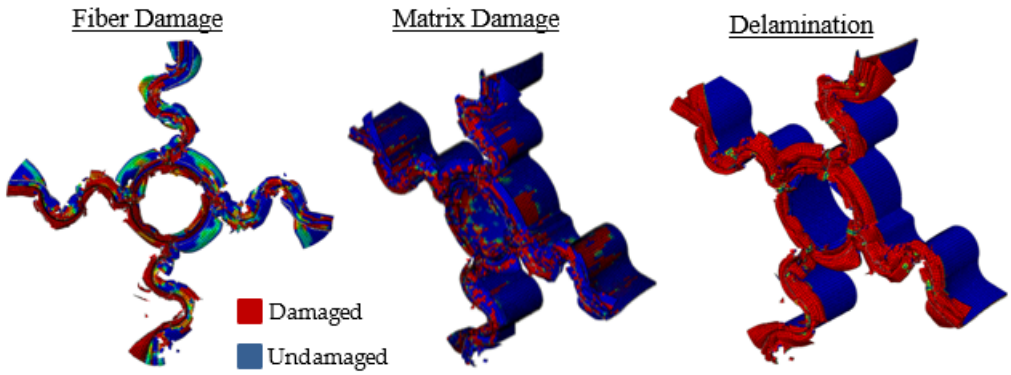

Figure 11. Simulation results of SL4 geometry.

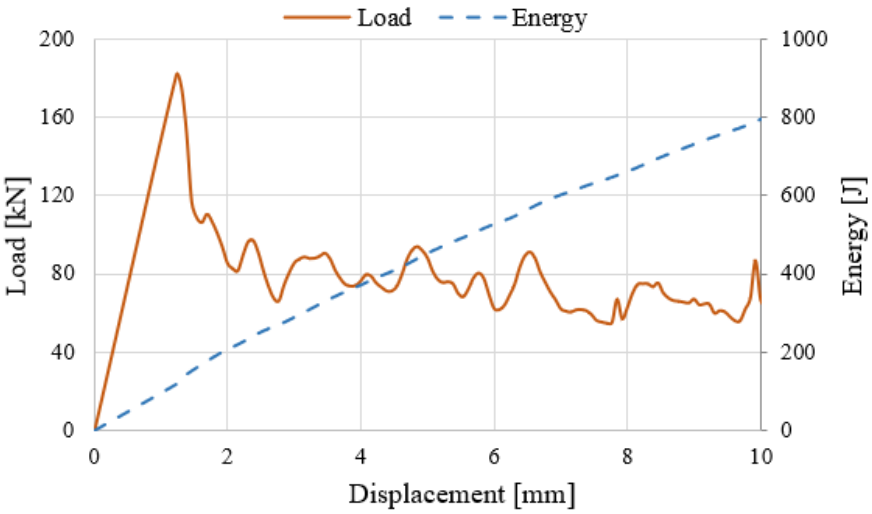

Figure 12. Load–displacement and energy curves of SL4 geometry.

The crushing modes observed in the SL8 geometry are depicted in Figure 13. The failure mechanisms closely resemble those of the previous geometry, as both designs feature

sinusoidal arms connected to a circular core. In the SL8 geometry, however, the sinusoidal plates are positioned closer to each other, resulting in intertwining damaged plies that elevate fiber fracture levels near the T-joints, consequently enhancing SEA performance. Nevertheless, given that fibers near the T-joints are already significantly fractured, the increase in SEA value is expected to be less substantial compared to the energy absorption capability of the SL4 geometry. The load–displacement curve and the energy curve of the SL8 geometry obtained by the simulation are illustrated in Figure 14.

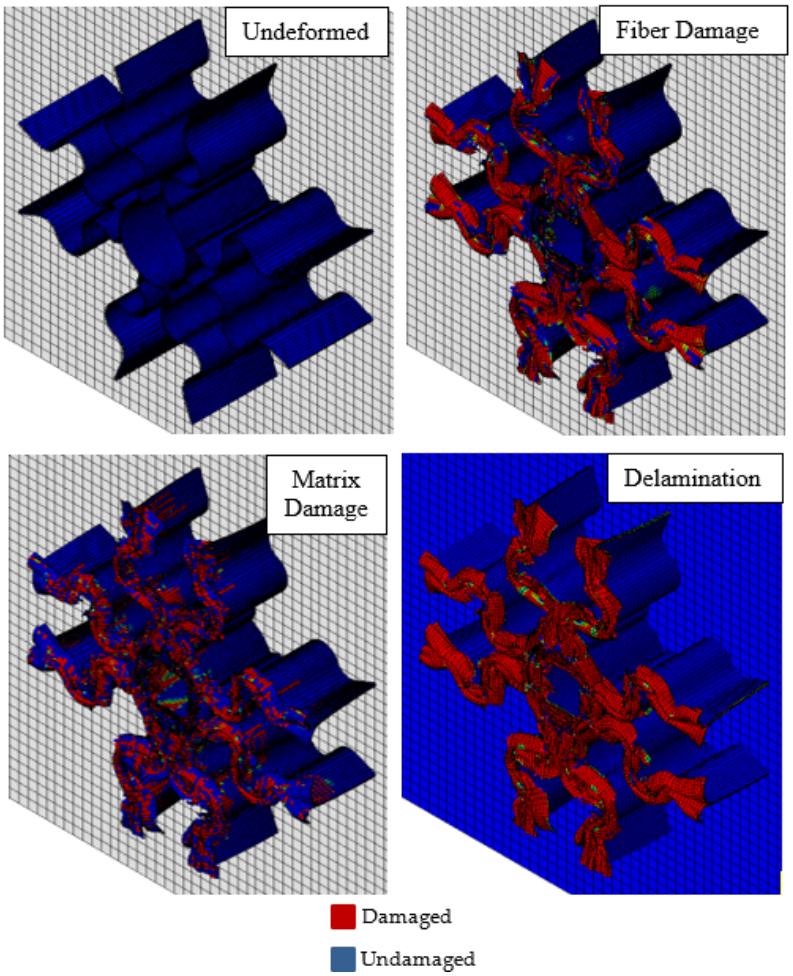

Figure 13. Simulation results of SL8 geometry.

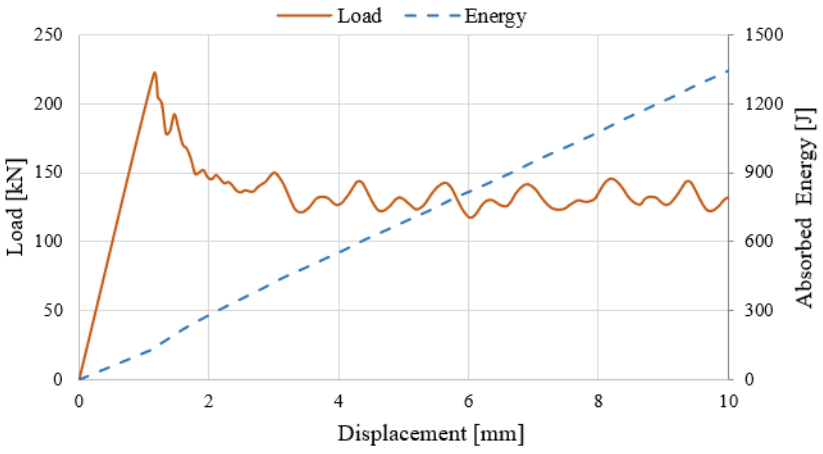

Figure 14. Load–displacement and energy curves of SL8 geometry.

Table 4 displays SEA results, along with the mass of the crushed specimen and the absorbed energy at the conclusion of the crushing process. The results indicate that PSP geometry does not offer a substantial increase in SEA performance compared to the single sinusoidal plate. This can be attributed to the presence of flat parts, which offset the performance enhancements provided by the T-joints. Conversely, the sun-like shapes featuring a circular core demonstrate a significant advantage in terms of energy absorption capability over both the single sinusoidal plate and the PSP geometry. Specifically, the SL4 geometry can absorb 16% more energy per unit mass than the single sinusoidal plate, while the SEA of the SL8 geometry is increased by 20%.

Table 4. Comparison of the numerical SEA results of designed geometries.

Geometry	Crushed Distance [mm]	Crushed Mass [g]	Absorbed Energy [J]	SEA [J/g]
Single Sinusoidal	10	3.63	249.41	68,72
PSP	10	7.62	521.08	70.64
SL4	10	9.65	769.15	79.70
SL8	10	16.45	1358.02	82.55

The results suggest that the sun-like geometry serves as a promising candidate for an energy-absorbing crash box structure. Between the two structures featuring 4 and 8 sinusoidal arms, there is negligible difference in terms of energy absorption capability. Thus, manufacturability emerges as a crucial criterion in determining the preferred structure. Considering the shape and number of molds required for manufacturing, as well as the subsequent laying up procedure, it is concluded that the SL4 geometry is preferable over the SL8 structure for achieving defect-free production.

3.3. Tapering

In addition to the energy absorption capacity, the initial peak load observed in the load–displacement curves of crash boxes under axial crushing poses a significant concern, as it can result in excessive deceleration and potentially fatal damage to passengers. Tapering the structures presents a potential solution to mitigate the peak load. Figure 15 illustrates the Abaqus/CAE model of the tapered SL4 geometry. In this configuration, the sinusoidal arms of the SL4 specimen are tapered by 5°, starting from the T-joints at the end of the circular core, resulting in a truncated conical geometry.

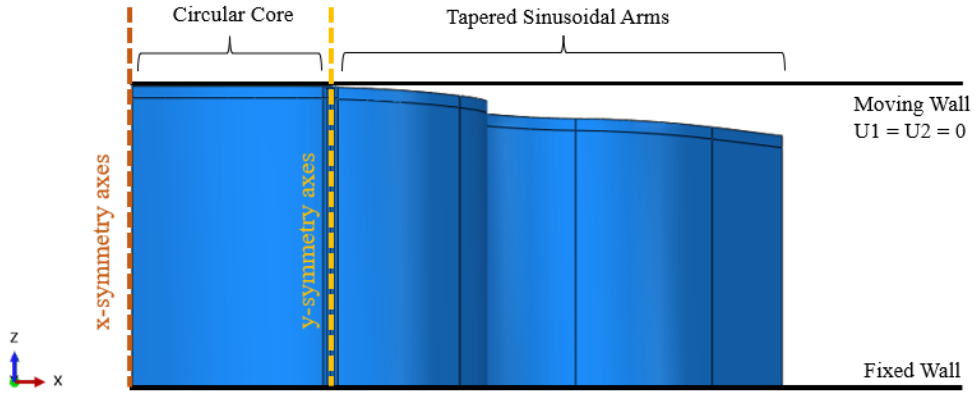

Figure 15. Abaqus/CAE model of tapered SL4 geometry.

The FEA model of the tapered structure comprises four sub-laminates, each meshed with continuum shell elements (SC8R) at a size of 1 × 1 mm^2. The imposed velocity and

boundary conditions remain consistent with the previous models. Figure 16 presents a comparison of the simulation results between the tapered SL4 geometry and the non-tapered version. The load–displacement curve illustrates a gradual upward trend in the first 3 mm, rather than a rapid buildup of peak load. Figure 17 depicts the progressive deformation and step-by-step growth of matrix cracks.

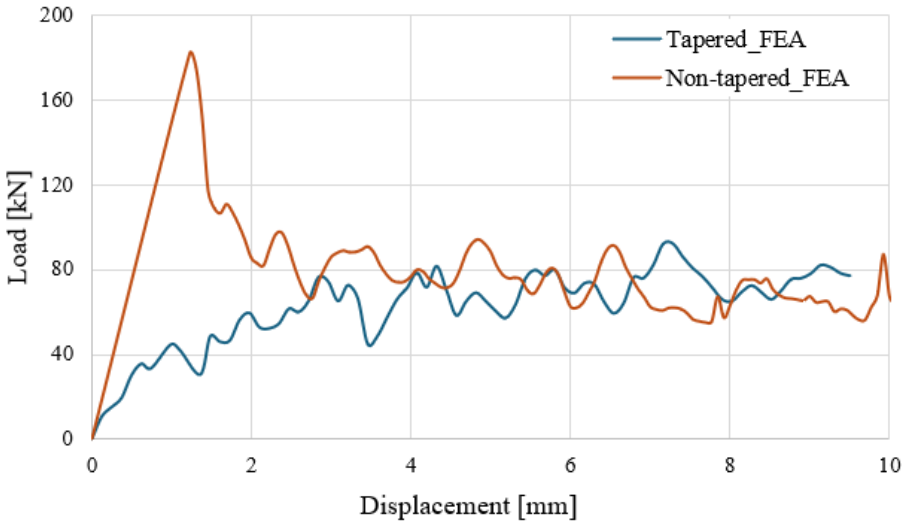

Figure 16. Load–displacement curves of tapered and non-tapered SL4 geometry.

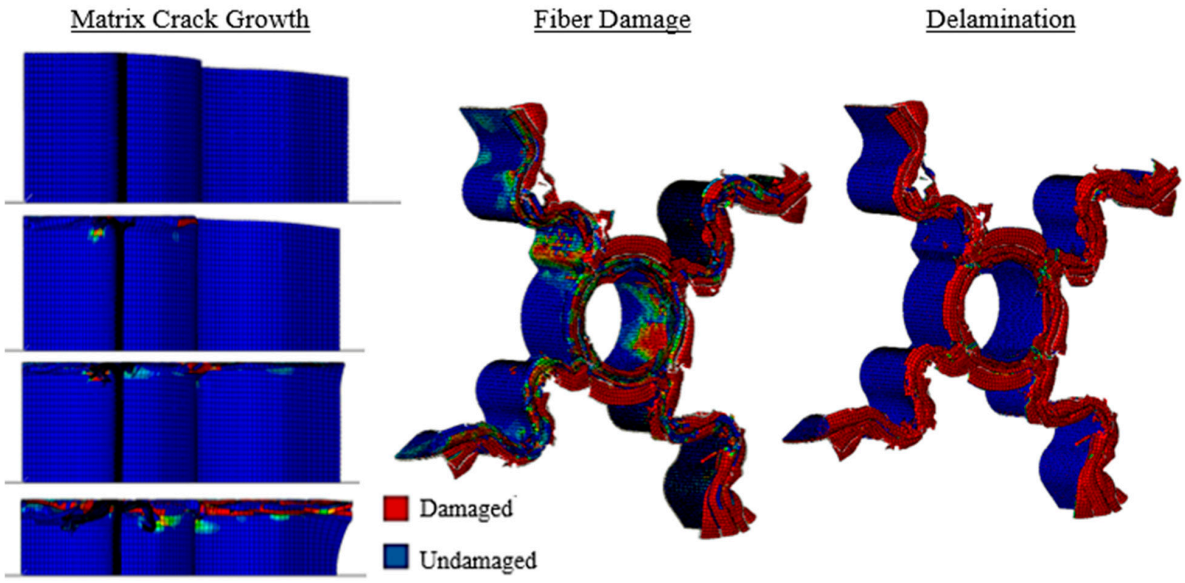

Figure 17. Simulation results of tapered SL4 geometry.

4. Manufacturing and Testing of the SL4 Geometry Made of UD Prepregs

The sun-like geometry with 4 arms is fabricated using AS4/8552 carbon-epoxy unidirectional (UD) prepregs supplied by HEXCEL, West Valley, UT, USA. via the hand lay-up technique. A custom-designed split die mold manufactured from a steel block using wire electro-discharge machining is used. During the composite part manufacturing process, a total of 8 plies of prepregs are stacked in a $[0/90]_{2s}$ cross-ply configuration: 4 layers are placed on the custom-made curved surfaces of four mold parts in a [0/90/0/90] configuration, while the remaining 4 layers are placed on a cylindrical tube positioned in the center, in a [90/0/90/0] configuration. Subsequently, the molds are sealed and vacuum-bagged, and the manufacturing process is finalized in an autoclave. Figure 18 provides snapshots illustrating the assembly of mold parts with the prepregs laid on them.

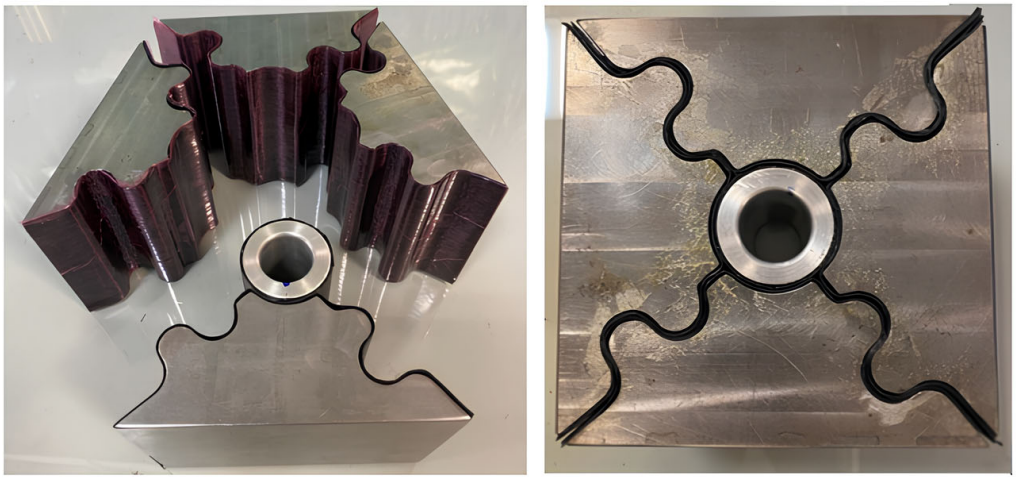

Figure 18. Snapshots taken during the manufacturing process.

After vacuum bagging and curing in the autoclave following the manufacturer's recommended cure cycle, four specimens are manufactured by cutting 50 mm in length and applying the chamfer to the edges. One of the specimens is tapered by 5° using a diamond disk cutter and grinding afterward with an emery paper. Specimens are tested in axial compression at a quasi-static speed of 1 mm/min by using the MTS hydraulic testing machine with a load capacity of 500 kN. Figure 19 demonstrates the final product and the test setup.

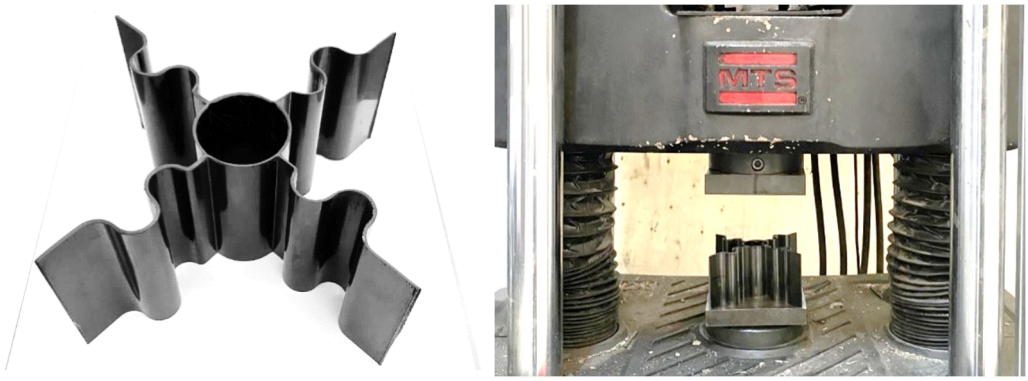

Figure 19. Manufactured sun-like geometry (**left**) and the test setup (**right**).

The crushed morphology of the untapered geometry at the end of the compression test is presented in Figure 20. Figure 21 demonstrates the experimental data (load–displacement curves) compared with the numerical predictions. According to the three repeated compression tests, SEA values of 78.30, 79.10, and 80.98 J/g are calculated, resulting in an average SEA of 79.46 J/g with a standard deviation of 0.95 J/g. Results indicate good repeatability and low difference among each test. More importantly, the experimental results show good consistency with the numerical estimations.

The test results for the tapered geometry made of UD prepregs are presented and compared with the numerical analysis in Figure 22. The results indicate that tapering effectively eliminates the peak load while still allowing the load to fluctuate around the same mean value as the original geometry after a certain distance of crash. Although the area under the curve decreased due to the change in the load–displacement trend, the SEA value of the tapered geometry remains close to that of the original geometry because the amount of material has also decreased for the first 5 mm. The SEA value of the manufactured tapered geometry made of UD prepregs is calculated to be 78.63 J/g.



Figure 20. The deformed shape of untapered SL4 geometry made of UD prepregs.

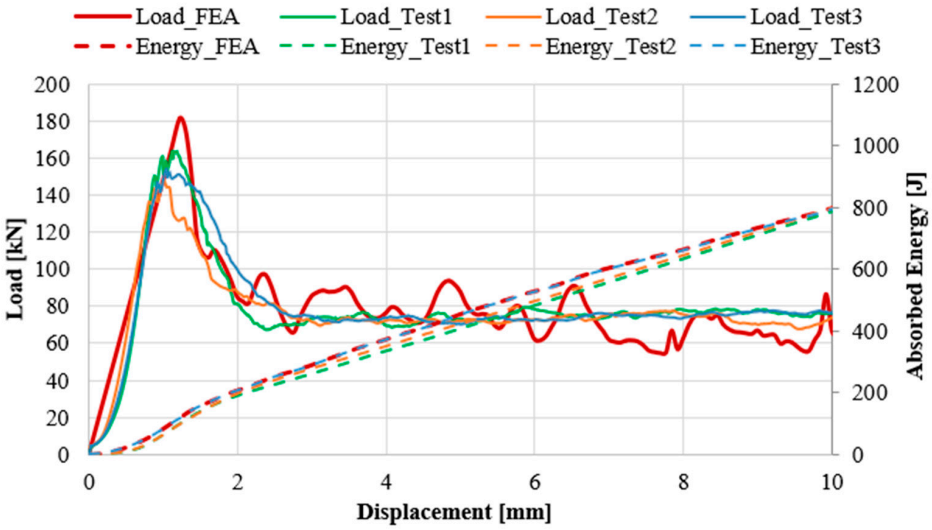

Figure 21. The experimental results of SL4 geometry made of UD prepregs compared with the numerical results.

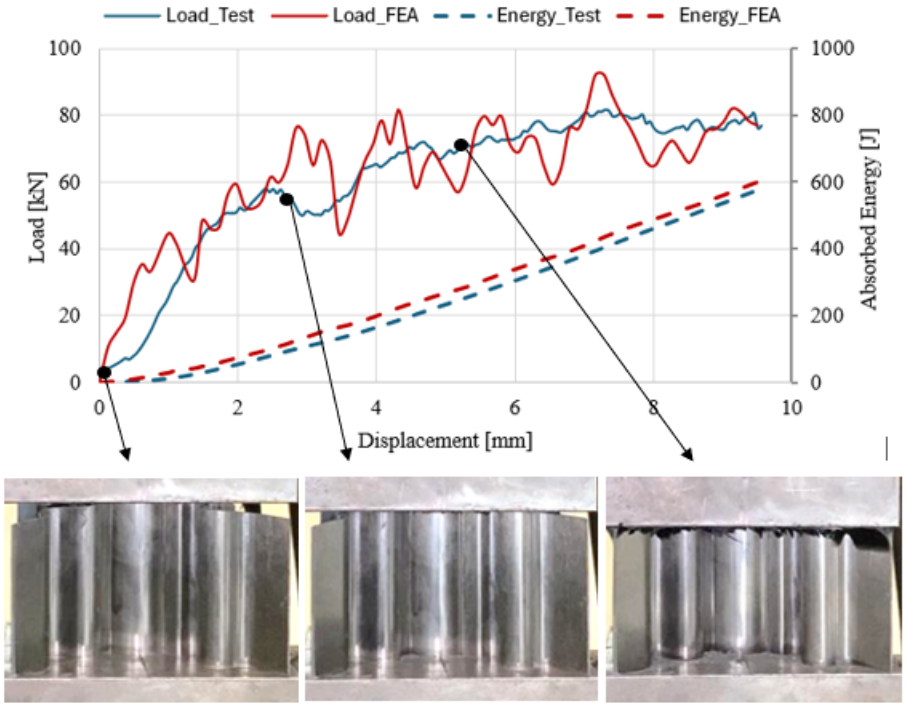

Figure 22. Comparison of the experimental and numerical results of tapered SL4 structure made of AS4/8552 UD prepregs: load–displacement and energy curves (**top**) and crushing sequence (**bottom**).

5. Numerical and Experimental Analysis of CFRP SL4 Geometry Made of WF Prepregs

Structures made of woven fabric prepregs, due to their textile nature obtained by interlocking yarns, are expected to exhibit much more complex failure mechanisms with more fiber damage and thus higher energy absorption capability. Hence, the SL4 geometry which gives the optimum SEA value is also manufactured using a woven fabric prepreg to compare the crushing performance.

The CFRP woven prepregs designated as KOM10T/PL200 utilized to fabricate the crash structures examined in this study are supplied by KORDSA, İstanbul, Turkey. They consist of plain weave 3K T300 carbon fibers manufactured by Toray, combined with an epoxy resin comprising 42% by weight. The areal weight of the prepregs is 200 g/m^2, and the cured ply thickness is 0.21 mm. At the same time, the crushing behavior of the SL4 geometry made of woven fabric prepregs is simulated in ABAQUS/Explicit to see the influence of prepreg type on SEA. Six plies of woven carbon fiber reinforced polymer (CFRP) layers, each with a thickness of 0.21 mm, are created and individually meshed using 1.0 × 1.0 mm planar continuum shell elements (SC8R). The composite structure is extruded as a full-scale model with a height of 50 mm. The imposed velocity and boundary conditions remain consistent with the UD model presented previously.

The plain weave composite prepregs used in this study exhibit very similar characteristics to those used by Zhou et al. [25], hence the material properties provided by Zhou et al. are adopted in this study. The material properties of the prepreg are outlined in Table 5. Intralaminar damage is defined using the built-in ABQ_PLY_FABRIC subroutine material model, and interlaminar damage is modeled using the Cohesive Zone Method (CZM). The ABQ_PLY_FABRIC subroutine treats each ply as a homogeneous orthotropic material, exhibiting progressive stiffness degradation due to fiber/matrix damage [25].

Table 5. Material properties used in the simulation of KOM10T/PL200 WF prepregs [25].

Description	Symbol	Unit	Value
Density	ρ	g/cm^3	1.56
Young modulus along fiber direction 1	E_1	GPa	65.1
Young modulus along fiber direction 2	E_2	GPa	64.4
Shear modulus	G_{12}	GPa	4.5
Principal Poisson ratio	v_{12}	-	0.37
Tensile strength along fiber direction 1	X_{1+}	MPa	776
Compressive strength along fiber direction 1	X_{1-}	MPa	704
Tensile strength along fiber direction 2	X_{2+}	MPa	760
Compressive strength along fiber direction 2	X_{2-}	MPa	698
Shear stress at the initiation of shear damage	S	MPa	95
Tensile fracture energy per unit area along fiber direction 1	G_f^{1+}	kJ/m^2	125
Compressive fracture energy per unit area along fiber direction 1	G_f^{1-}	kJ/m^2	250
Tensile fracture energy per unit area along fiber direction 2	G_f^{2+}	kJ/m^2	95
Compressive fracture energy per unit area along fiber direction 1	G_f^{2-}	kJ/m^2	245
Initial effective shear yield strength	$\tilde{\sigma}_{y0}$	MPa	185
Interfacial strength (Mode I)	τ_I	MPa	54
Interfacial strength (Mode II and III)	$\tau_{II} = \tau_{III}$	MPa	70
Fracture toughness (Normal)	G_{Ic}	[kJ/mm^2]	0.504
Fracture toughness (Shear)	$G_{IIc} = G_{IIIc}$	[kJ/mm^2]	1.56

Three tapered WF SL4 geometries are manufactured by stacking 6 plies of woven fabric prepreg on the same steel molds utilized to produce sun-like geometry. Since the overlapping molds were designed according to a wall thickness of 1.47 mm using 8 layers of UD prepreg with cured ply thickness of 0.184 mm, six plies of WF prepreg with a cured

ply thickness of 0.21 mm were laid in the mold to obtain a wall thickness of 1.26 mm, and the gap is filled by laying 0.2 mm thick Teflon film on the mold surfaces. The molds are vacuum bagged, and then the manufacturing process was completed again in the autoclave according to the manufacturer's recommended cure cycle. The specimens are cut to 50 mm in length, and the edges are tapered. The tapered structures are finally tested at a quasi-static speed of 1 mm/min. Figure 23 demonstrates the final structure made of WF prepregs.

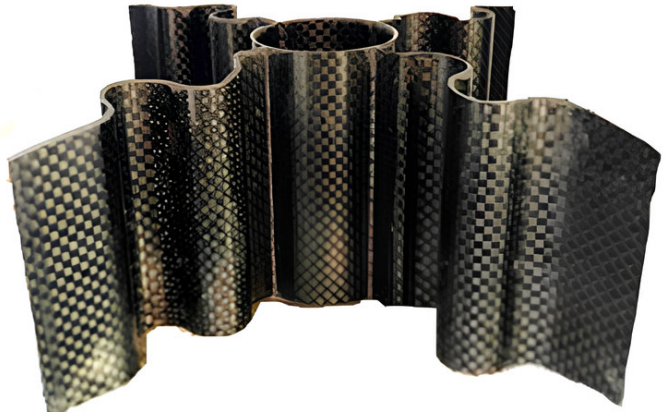

Figure 23. The sun-like tapered structure made of WF prepregs.

Figure 24 presents the numerical and experimental results of the tapered sun-like structures made of woven fabric (WF) prepregs. Compared to the UD structures, WF specimens show better energy absorption performance during crushing. Calculated SEA values of 89.10, 87.73, and 90.96 J/g for three specimens result in the average value of 89.26 J/g with a standard deviation of 1.62 J/g. The increased energy absorption is attributed to the textile nature of the WF prepregs, where the interlocking yarns result in more fragmentation rather than a splaying mode. A great level of agreement can be also observed between the experimental results and the numerical estimations. FE simulations give the SEA value of 91.21 J/g. Figure 25 illustrates the deformed shape at the end of both the numerical and experimental procedures.

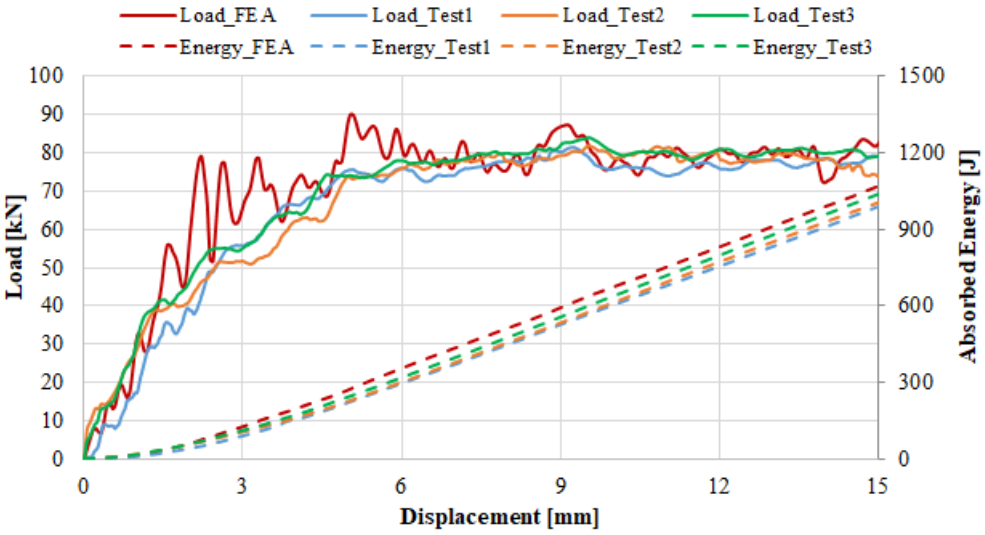

Figure 24. Comparison of the experimental and numerical results of tapered SL4 structure made of KOM1OT/PL200 WF prepregs: load–displacement and energy curves.

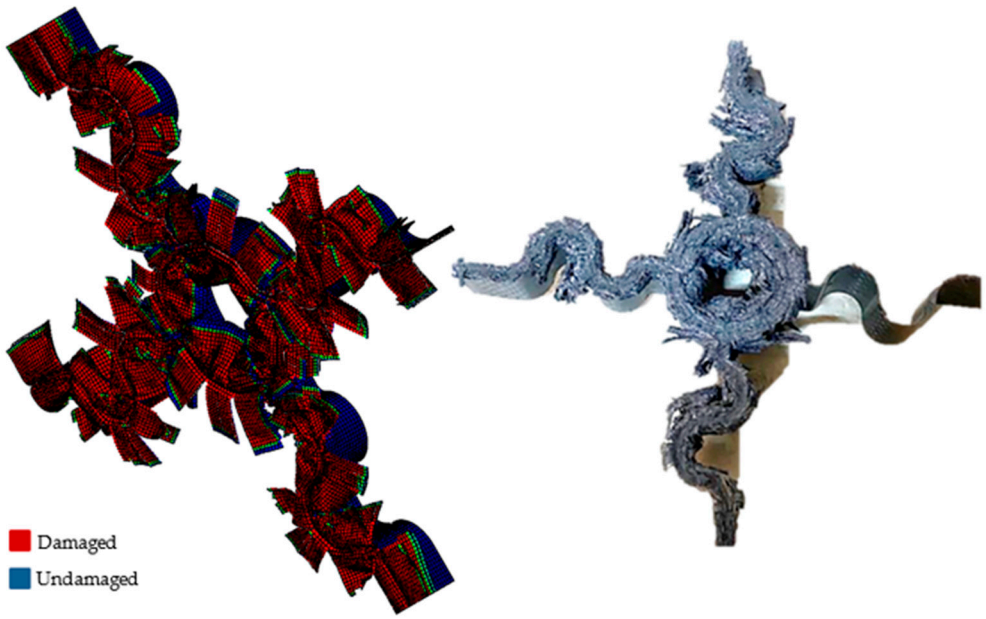

Figure 25. The deformed shapes of sun-like geometry made of WF prepregs at the end of the simulation (**left**) and quasi-static crushing test (**right**).

6. Conclusions

In this paper, a comprehensive design investigation was conducted to develop a novel CFRP crash box geometry with enhanced SEA performance. The proposed design concept involves assembling sinusoidal plates through T-shaped joints, which creates obstacles to delamination, thereby increasing fragmentation and increasing the amount of energy absorbed during the crushing process. Several design iterations were analyzed in ABAQUS/Explicit using the proposed computationally efficient numerical approach. The results demonstrated that sun-like shapes with a circular core offered a significant advantage in energy absorption capability over both the parallel sinusoidal plate design and the single sinusoidal structure. Although the sun-like structure with eight half sinusoidal arms showed slightly better performance than the four-arm configuration, the latter was selected as the optimal design due to the manufacturing complexity and part quality considerations.

Quasi-static compression tests performed on the selected sun-like geometry confirmed the numerical predictions, yielding an average SEA of 79.46 J/g, which represents a 16% improvement relative to the single sinusoidal plate. Moreover, tapering the edges of the crash box structure to form a conical shape effectively eliminated the initial peak load while preserving the overall SEA performance.

In the final phase of this study, the optimal geometry was further simulated and manufactured using WF prepregs, resulting in an increased average SEA of 89.26 J/g, which is 12.4% higher than the structure mode of unidirectional prepregs and 29.8% higher than the single sinusoidal structure. The overall SEA comparison obtained from both the numerical and experimental results is summarized in Figure 26.

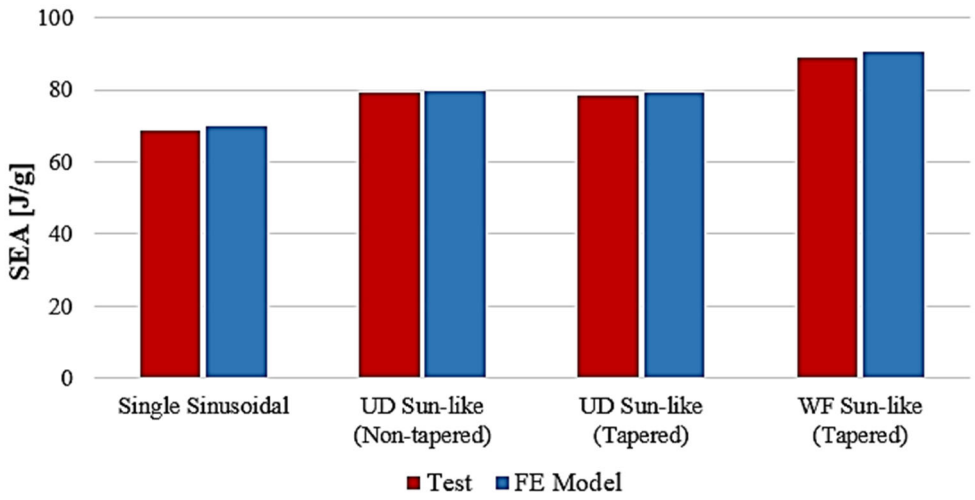

Figure 26. The overall SEA comparison.

Author Contributions: M.E.: Conceptualization, Investigation, Methodology, Validation, Software, Writing—original draft. S.D.: Methodology, Validation, Software. N.E.: Methodology, Supervision, Writing—review and editing. All authors have read and agreed to the published version of the manuscript.

Funding: This work was supported by the Boğaziçi University Research Fund, with grant number 17621D.

Data Availability Statement: Data sharing is not applicable to this article.

Conflicts of Interest: The authors declare no conflicts of interest.

References

1. Bayu, A.; Koronka, K.; Kadarno, P.; Purbolaksono, P. Energy Absorption Analysis of Composite Crash Box by Finite Element Method. In Proceedings of the 1st International Conference on Contemporary Risk Studies, Jakarta, Indonesia, 31 March–1 April 2022.
2. Abada, M.; Ibrahim, A. Hybrid Multi-Cell Thin-Walled Tubes for Energy Absorption Applications: Blast Shielding and Crashworthiness. *Compos. Part B Eng.* **2020**, *18*, 107720. [CrossRef]
3. Mohammadi, H.; Ahmad, Z.; Mazlan, S.A. Lightweight Glass Fiber-Reinforced Polymer Composite for Automotive Bumper Applications: A Review. *Polymers* **2023**, *15*, 193. [CrossRef] [PubMed]
4. Demir, S.; Ersoy, N.; Engül, M.C. Axial Quasi-Static Crushing of Composite Tubes: An Investigation on the Influence of the Modelling Techniques. *J. Reinf. Plast. Compos.* **2023**, *44*, 17–35. [CrossRef]
5. Abdullah, N.A.Z.; Sani, M.S.; Salwani, M.S.; Husain, N.A. A Review on Crashworthiness Studies of Crash Box Structure. *Thin-Walled Struct.* **2020**, *153*, 106795. [CrossRef]
6. Kindervater, C.M. Energy Absorption of Composites as an Aspect of Aircraft Structural Crash-Resistance. In *Developments in the Science and Technology of Composite Materials*; Springer: Dordrecht, The Netherlands, 1990; pp. 643–651.
7. Mamalis, A.; Robinson, M.; Manolakos, D.; Demosthenous, G.; Ioannidis, M.; Carruthers, J. Review: Crashworthy Capability of Composite Material Structures. *Compos. Struct.* **1997**, *37*, 109–134. [CrossRef]
8. Farley, G. Effect of Specimen Geometry on the Energy Absorption Capability of Composite Materials. *J. Compos. Mater.* **1986**, *20*, 390–400. [CrossRef]
9. Farley, G.; Jones, R. Crushing Characteristics of Composite Tubes with "Near Elliptical" Cross Sections. *J. Compos. Mater.* **1992**, *12*, 1741–1751. [CrossRef]
10. Hussain, N.; Regalla, S.P.; Rao, Y.V.D.; Dirgantara, T.; Gunawan, L.; Jusuf, A. Drop-Weight Impact Testing for the Study of Energy Absorption in Automobile Crash Boxes Made of Composite Material. *Mater. Des. Appl.* **2020**, *235*, 114–130. [CrossRef]
11. Hanagud, S.; Craig, I.; Sriram, P.; Zhou, W. Energy Absorption Behavior of Graphite Epoxy Composite Sine Webs. *J. Compos. Mater.* **1989**, *23*, 448–459. [CrossRef]

12. Wiggenraad, J.F.; Santoro, D.; Lepage, F.; Kindervater, C.M.; Mañez, H.C. *Development of a Crashworthy Composite Fuselage Concept for a Commuter Aircraft*; NLR-TP-2001-108; National Aerospace Laboratory NLR: Emmeloord, The Netherlands, 2001. Available online: https://reports.nlr.nl/server/api/core/bitstreams/4a213884-8809-46a7-8647-31ea13fa5a05/content (accessed on 30 January 2026).
13. Sokolinsky, V.S.; Indermuehle, K.C.; Hurtado, J.A. Numerical Simulation of the Crushing Process of a Corrugated Composite Plate. *Compos. Part A Appl. Sci. Manuf.* **2013**, *42*, 1119–1126. [CrossRef]
14. Engül, M.C.; Ersoy, N. From Flat Plates to Sinusoidal Structures: Influence of Geometry on the Energy Absorption Capability of Carbon/Epoxy Composites. *J. Compos. Sci.* **2023**, *7*, 56. [CrossRef]
15. Engül, M.C.; Demir, S.; Ersoy, N. The Influence of Geometry on the Energy Absorption Capability of Composite Structures Made of Woven Fabric Prepregs. In Proceedings of the 23rd International Conference on Composite Materials (ICCM/23), Belfast, Northern Ireland, 30 July–4 August 2023.
16. Jimenez, M.; Larrode, E.; Revuelta, D. Effect of Trigger Geometry on Energy Absorption in Composite Profiles. *Compos. Struct.* **2000**, *48*, 107–111. [CrossRef]
17. Engül, M.C.; Öz, F.E.; Ersoy, N. Experimental and Numerical Investigation of the Crushing Process of Composite Crash Box. In Proceedings of the 21st International Conference on Composite Materials (ICCM/21), Xi'an, China, 20–25 August 2017.
18. Liu, Q.; Fu, J.; Ma, Y.; Zhang, Y.; Li, Q. Crushing Responses and Energy Absorption Behaviors of Multi-Cell CFRP Tubes. *Thin-Walled Struct.* **2020**, *155*, 106930. [CrossRef]
19. Wu, F.; Chen, Y.; Zhao, S.; Hong, Y.; Zhang, Z.; Zheng, S. Mechanical Properties and Energy Absorption of Composite Bio-Inspired Multi-Cell Tubes. *Thin-Walled Struct.* **2023**, *18*, 110451. [CrossRef]
20. Engül, M.; Ersoy, N. Energy Absorption Capability of Carbon/Epoxy Composite Laminates: A Novel Numerical Approach. *J. Reinf. Plast. Compos.* **2023**, *42*, 1262–1276. [CrossRef]
21. Hashin, Z. Failure Criteria for Unidirectional Fibre Composites. *J. Appl. Mech.* **1980**, *47*, 329–334. [CrossRef]
22. Lubineau, G. On a Damage Mesomodel for Laminates: Micro–Meso Relationships, Possibilities and Limits. *Compos. Sci. Technol.* **2001**, *61*, 2149–2158.
23. Camanho, P.P.; Davila, C.G.; Moura, M.F. Numerical Simulation of Mixed-Mode Progressive Delamination in Composite Materials. *Mater. Sci. Eng. Compos.* **2003**, *47*, 1415–1438. [CrossRef]
24. ABAQUS/Standard User's Manual, ver. 6.14. Dassault Systèmes SIMULIA Corp: Providence, RI, USA, 2024. Available online: https://www.3ds.com/support/documentation (accessed on 30 January 2026).
25. Zhou, G.; Sun, G.; Li, G.; Cheng, A.; Li, Q. Modelling for CFRP Structures Subjected to Quasi-Static Crushing. *Compos. Struct.* **2018**, *184*, 41–55. [CrossRef]

Disclaimer/Publisher's Note: The statements, opinions and data contained in all publications are solely those of the individual author(s) and contributor(s) and not of MDPI and/or the editor(s). MDPI and/or the editor(s) disclaim responsibility for any injury to people or property resulting from any ideas, methods, instructions or products referred to in the content.